

# Interleaved bond and magnetic frustration in triangular lattice $LnCd_3P_3$

S. J. Gomez Alvarado,<sup>1,\*</sup> J. R. Chamorro,<sup>1,\*</sup> A. R. Jackson,<sup>1</sup> G. Pokharel,<sup>1</sup> R. Gomez,<sup>1</sup> B. R. Ortiz,<sup>1</sup> Suchismita Sarker,<sup>2</sup> L. Kautzsch,<sup>1</sup> L. C. Gallington,<sup>3</sup> R. Seshadri,<sup>1,4</sup> and Stephen D. Wilson<sup>1,†</sup>

<sup>1</sup>Materials Department, University of California, Santa Barbara, California 93106, USA

<sup>2</sup>Cornell High Energy Synchrotron Source, Cornell University, Ithaca, New York 14853, USA

<sup>3</sup>X-ray Science Division, Advanced Photon Source, Argonne National Laboratory, 9700 S. Cass Ave, Argonne, Illinois 60439, USA

<sup>4</sup>Materials Research Laboratory, University of California, Santa Barbara, California 93106, USA

We report the presence of frustrated bond order in the form of short-range charge correlations in the triangular lattice antiferromagnetic compounds  $LnCd_3P_3$  ( $Ln = La, Ce, Pr, \text{ and } Nd$ ). These compounds feature two-dimensional planes of trigonal-planar  $CdP_3$  units that separate tetrahedral  $CdP_4$  layers; collectively, these sandwich edge-sharing triangular lattice planes of  $LnP_6$  octahedra. Diffuse X-ray scattering data reveal an underlying bond instability within the unique  $CdP_3$  units that breaks rotational symmetry along one  $Cd-P$  bond direction, with long-range ordering being frustrated via emergent kagome-ice bond correlations. Our results establish  $LnCd_3P_3$  as a rare class of materials where frustrated magnetism across a tunable rare-earth triangular network is embedded within a dopable semiconductor with a frustrated bond order instability.

## I. INTRODUCTION

Geometrical frustration on triangular lattice networks can lead to number of unconventional states arising from the competition between electronic degrees of freedom. Magnetic interactions, for example, across the triangular lattice network are predicted to stabilize states such as the quantum spin liquids or native quantum disordered ground states [1–12]. This frustration is, however, not limited to spin interactions, and the charge degree of freedom can also be impacted via forms of orbital or bond frustration [13–18].

Interfacing the charge degree of freedom with highly frustrated magnetic states is an experimental challenge in the field of quantum materials. Creating such an interface is key to testing many of predictions of unconventional superconductivity, quantum criticality, and other phenomena that are predicted to arise when itinerant charge carriers interact within a fluctuating background of entangled spins [19–26]. However, many of the leading materials candidates hosting a highly frustrated magnetic lattice are built from highly localized lanthanide ( $Ln$ ) ions whose charge degree of freedom is strongly gapped out and are not readily dopable [1]. Conversely, many dopable magnetic materials are often built from transition metal ions that possess extended exchange interactions or other interactions that lower crystallographic symmetries and lift magnetic frustration [27–29]. Bridging this divide and establishing a cleanly tunable material platform that allows for conduction electrons to coexist within a frustrated, local moment lattice network remains an important goal.

There has been recent progress in stabilizing quantum disordered or quantum spin liquid states across triangular lattice networks of  $S_{\text{eff}} = 1/2$  magnetic moments

derived from lanthanide ( $Ln$ ) ions. A number of quantum disordered or nearly disordered states have been reported in layered  $ALnX_2$  compounds for instance [3, 30–37]; however doping itinerant charge carriers into these large gap insulators is a challenge. In the pursuit of an alternative platform that can host a similar triangular lattice network of  $Ln$  moments with a smaller, dopable semiconductor charge gap, the  $Ln(Cd,Zn)_3(P,As)_3$  family of compounds presents a number of interesting candidates [38–56].

$Ln(Cd,Zn)_3(P,As)_3$  compounds, based on the prototypical  $ScAl_3C_3$  structure type, host an ideal triangular lattice of rare-earth moments whose anisotropies and ground states can be tuned via  $Ln$  composition. There is also evidence that they are tunable semiconductors that can be driven from insulators into metals via steric effects [40] or via slight self-doping effects during crystal growth [42]. In contrast to the delafossite-variant  $ALnX_2$  compounds, strong covalency between the transition metal and pnictide ions leads to a highly disperse valence band, likely enabling  $p$ -type doping [39, 47, 56]. An important open question is whether the carriers in these compounds, derived mainly from the transition metal-pnictide interstitial layers, experience comparable frustration effects and whether additional charge or bond order instabilities can be interfaced with the frustrated  $Ln$  network.

In this paper, we demonstrate that the  $LnCd_3P_3$  family of compounds hosts a highly frustrated lattice instability via the formation of local bond order across a honeycomb network rooted in distorted trigonal-planar  $CdP_3$  layers within the unit cell. A combination of single-crystal diffuse X-ray scattering and powder pair distribution function analyses identify a local shortening of  $2/3$  of the trigonal  $Cd-P$  bonds, resulting in the formation of one-dimensional  $CdP$  chains which are prevented from forming long-range order via geometric frustration in a manner analogous to kagome-ice correlations [57]. Interactions between these distortions can be mapped to a frustrated tiling of dimers across a honeycomb network

\* These authors contributed equally to this work.

† stephendwilson@ucsb.edu

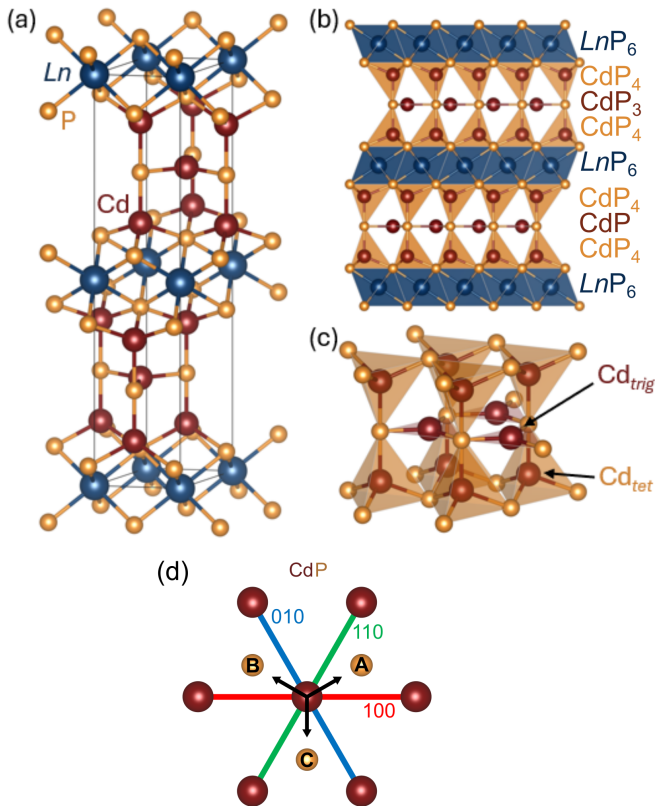


FIG. 1. (a) The  $\text{ScAl}_3\text{C}_3$ -type structure of  $\text{LnCd}_3\text{P}_3$  (space group  $P6_3/mmc$ ). (b) The structure is composed of alternating layers of  $\text{LnP}_6$  octahedra,  $\text{CdP}_4$  tetrahedra, and  $\text{CdP}_3$  trigonal planar units. (c) We distinguish the trigonal planar and tetrahedral Cd sites as  $\text{Cd}_{\text{trig}}$  and  $\text{Cd}_{\text{tet}}$ , respectively. (d) The distortion modes observed in the local structure involve the displacement of the  $\text{Cd}_{\text{trig}}$  and  $\text{P}_{\text{trig}}$  sites along one of three equivalent Cd-P bond directions (labeled A, B, and C).

[58, 59], leading to fluctuating orthorhombic domains which locally break the in-plane rotational and translational symmetry.

Our results establish the  $\text{LnCd}_3\text{P}_3$  family of triangular lattice antiferromagnets as a rare material platform where frustration of the charge degree of freedom can be interfaced with frustrated magnetism within the same lattice framework, and we further suggest that the unidentified order resolved in previous studies of metallic  $\text{LnCd}_3\text{P}_3$  [42] and  $\text{LnCd}_3\text{As}_3$  crystals [49] is a partial freezing of this bond order.

## II. EXPERIMENTAL DETAILS

### A. Sample synthesis

Single crystals of  $\text{LnCd}_3\text{P}_3$  were prepared from a molten salt flux [38]. A stoichiometric amount of elemental  $\text{Ln}$  powder (Fisher Scientific, 99.9% REO),  $\text{Cd}_3\text{P}_2$  powder (Alfa Aesar, 99.5% metals basis), and red P

(BeanTown Chemical, 99.9999%) was combined in a total of 500 mg of solute powder. This powder was then sealed in an evacuated silica ampoule with 2 g of 1:1 molar ratio of KCl and NaCl salts. The silica ampoule was then heated at  $50^\circ\text{C/hr}$  to  $900^\circ\text{C}$ , where it dwelled for 72 hours. Then, it was slowly cooled to  $660^\circ\text{C}$  at  $2^\circ\text{C/hr}$ , then allowed to furnace cool to room temperature. To retrieve the samples, the silica ampoules were first scored and opened above the solidified salt. The section of the ampoule with the solidified salt was then placed in a beaker full of deionized water on a hot plate so the salt could be dissolved. As the salt dissolved, the crystals and other products would accumulate at the bottom of the beaker. Most of the excess dissolved salt and water were discarded, and the crystals and products were examined and extracted.

Polycrystalline samples were prepared using conventional solid-state synthetic techniques [41]. First,  $\text{LnP}$  precursors were prepared by direct reaction of elemental rare earth powders with red P. Stoichiometric amounts of the elements were weighed and ground together in an Ar-filled glovebox, followed by heating in alumina crucibles at  $850^\circ\text{C}$  for 48 hours in sealed, evacuated silica ampoules. These precursors were then combined with a stoichiometric amount of  $\text{Cd}_3\text{P}_2$ , and ball milled in a Spex 8000D Mixer/Mill for 1 hour using a tungsten carbide vial and tungsten carbide balls. The milled mixture was then sealed in an evacuated silica ampoule and heated to  $800^\circ\text{C}$  for 24 hours before being quenched in water.

### B. X-ray scattering measurements

Powder pair distribution function (PDF) datasets were collected at the 11-ID-B beamline of the Advanced Photon Source (APS), Argonne National Laboratory, with an incident wavelength of  $0.1432 \text{ \AA}$ . Data were collected at  $T = 80 \text{ K}$  and  $300 \text{ K}$ , and PDF patterns were extracted with a maximum momentum transfer of  $|Q|_{\text{max}} = 25 \text{ \AA}^{-1}$ . Modeling and fitting of the PDF data were performed using TOPAS ACADEMIC [60] and ISODISTORT [61].

Temperature-dependent single crystal synchrotron X-ray diffraction experiments were performed at the QM<sup>2</sup> beamline at the Cornell High Energy Synchrotron Source (CHESS). To avoid the absorption edges of constituent elements, an incident X-ray wavelength  $\lambda = 0.676 \text{ \AA}$  ( $E = 26 \text{ keV}$ ) was chosen using a double-bounce diamond monochromator. A stream of cold He gas flowing across the crystal sample was used to control the temperature. A Pilatus 6M area detector array collected the scattering intensities in transmission geometry, and data were collected while the samples were rotated with three tilted  $360^\circ$  rotations, sliced into  $0.1^\circ$  frames. Data were visualized and analyzed using the NXPY and NXS-ANALYSIS-TOOLS software suites [62, 63]. The viewing axes for the  $(H, K)$  scattering planes were skewed by  $60^\circ$

to reflect the relative orientation between the  $H$  and  $K$  axes.

### C. $\Delta$ -PDF analysis

The single crystal X-ray diffraction data were symmetrized using the symmetry operations belonging to the  $6/mmm$  ( $D_{6h}$ ) point group. The full three-dimensional scattering volume used for three-dimensional difference pair distribution function (3D- $\Delta$ PDF) analysis was defined by the limits  $H_{\max} = 4.5$ ,  $K_{\max} = 4.5$ , and  $L_{\max} = 8.5$ . The large background centered at the origin of reciprocal space was removed from the dataset by subtracting broad, three-dimensional Gaussian profiles. Pixels with counts below a chosen minimum were then filled in with a flat background prior to isolating the diffuse scattering. Bragg peaks and artifacts were removed from the dataset by defining an ellipsoidal volume around each integer ( $H, K, L$ ) coordinate, and any pixels within this volume possessing a value above a chosen threshold intensity were deleted. Resulting gaps in the data were then filled in via convolution with a Gaussian kernel. Care was taken to ensure that the kernel was circular in the ( $H, K$ ) scattering plane *after* a  $60^\circ$  skew of the axes, so that any smoothing effects would impart minimal distortions to the symmetry of the observed scattering. A hexagonal Tukey window was applied to the in-plane scattering with  $\alpha = 0.5$ . Along  $L$ , a standard Tukey window was applied with  $\alpha = 1.0$ . The viewing axes for the ( $x, y$ )  $\Delta$ PDF planes shown in this paper are skewed by  $120^\circ$  to reflect the angle between the crystallographic  $a$  and  $b$  axes.

### III. LOCAL STRUCTURE AND POWDER PDF

A representative unit cell for  $LnCd_3P_3$  is shown in Figure 1(a). The structure is composed of alternating layers of  $LnP_6$  octahedra,  $CdP_4$  tetrahedra, and  $CdP_3$  trigonal planar units [Fig. 1(b)]. The latter form a honeycomb pattern, with Cd and P alternating at the vertices, reminiscent of hexagonal BN and of the Zn(As/P) layer in hexagonal KZn(As/P)[64, 65] [Figure 1(c)]. Here we denote the two separate Cd crystallographic sites as  $Cd_{\text{trig}}$  and  $Cd_{\text{tet}}$ ; the P sites are denoted in a similar fashion.

In first examining the structure across the  $LnCd_3P_3$  compound series, refinement of average structural models using powder X-ray diffraction measurements reveal large anisotropic displacement parameters for the  $Cd_{\text{trig}}$  and  $P_{\text{trig}}$  sites in all four  $Ln = \text{La, Ce, Pr, and Nd}$  compounds. Data and refinements are shown in Figure 2. The values for the structural refinements are reported in the supplementary information (Table S1 [66]) and are consistent with a previous report of  $PrCd_3P_3$  [38]. In all four compounds,  $Cd_{\text{trig}}$  cations exhibit large displacements along the  $c$ -axis at room temperature, displacing toward the large voids above and below the site.

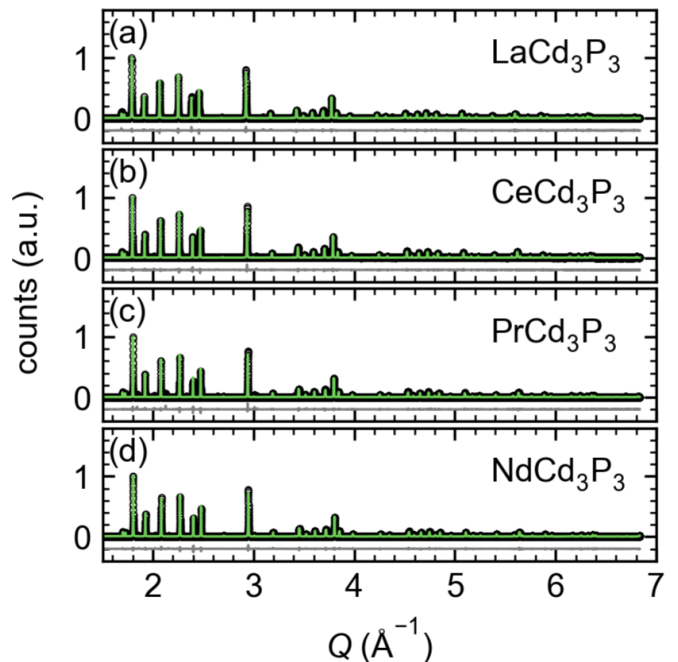


FIG. 2. Synchrotron powder X-ray diffraction data sets collected at  $T = 5$  K and hexagonal  $P6_3/mmc$  fits from Rietveld refinement for (a)  $LaCd_3P_3$ , (b)  $CeCd_3P_3$ , (c)  $PrCd_3P_3$ , and (d)  $NdCd_3P_3$ . Open circles represent raw data, and solid lines indicate fit and difference profiles.

$P_{\text{trig}}$  anions, on the other hand, have larger in-plane displacements at this temperature. Notably, upon cooling toward  $T = 5$  K, both the  $Cd_{\text{trig}}$  cation and  $P_{\text{trig}}$  anion displacements evolve to be strongly in-plane, revealing a tendency toward two-dimensional disorder within the  $ab$ -plane.

To explore this further, X-ray PDF measurements of the local structure of polycrystalline samples of  $LnCd_3P_3$  were performed at  $T = 80$  K [Fig. 3(a), Fig. S1 [66]] and 300 K (Fig. S2 [66]). Small-box modeling and fitting to the data reveal a preference for a distorted, orthorhombic  $Cmcm$  cell over the average hexagonal  $P6_3/mmc$  cell that is enhanced as the fitting range becomes more local [Fig. 3(c)]. The primary driver of the proposed distortion and resulting symmetry lowering is the breaking of rotational symmetry in the trigonal planar  $CdP_3$  units within the  $CdP$  layer. This suggests a local contraction of two of the three equivalent Cd-P bond lengths within the  $Cd_{\text{trig}}$  layers and a potential local bond order that is frustrated within the plane [Fig. 3(d,e)].

### IV. LOCAL BOND ORDER AND SINGLE-CRYSTAL $\Delta$ -PDF

To further study the presence of local symmetry lowering, single crystal synchrotron X-ray diffraction measurements were performed on crystals of  $LaCd_3P_3$ ,  $CeCd_3P_3$ ,  $PrCd_3P_3$ , and  $NdCd_3P_3$ . Because the data are qualita-

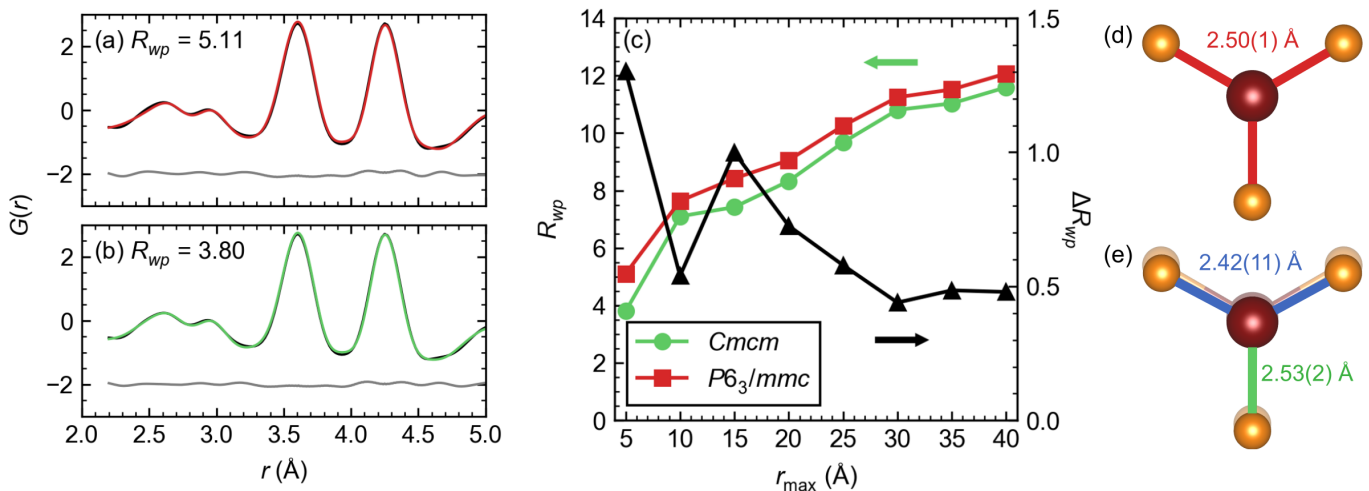


FIG. 3. Powder pair distribution function analysis for  $\text{PrCd}_3\text{P}_3$  at  $T = 80$  K. (a) Profile fit obtained from small-box modeling for the range  $2.2 \text{ \AA} < r < 5 \text{ \AA}$ , using the hexagonal  $P6_3/mmc$  cell and (b) the orthorhombic  $Cmc m$  cell. (c) Comparison of the  $R_{wp}$  values obtained over the ranges  $2.2 \text{ \AA} < r < r_{max}$  as a function of  $r_{max}$ . The right axis shows the difference between the  $Cmc m$  and  $P6_3/mmc$  fits for each  $r_{max}$ . (d) The refined bond lengths obtained from the  $P6_3/mmc$  and (e)  $Cmc m$  fits.

tively similar in reciprocal-space structure amongst all four compounds, a representative  $(H, K)$ -plane diffraction pattern for  $\text{PrCd}_3\text{P}_3$  is presented in Figure 4(a). Corresponding data for all four compounds are shown in Fig. S3 [66]. Aside from sharp Bragg peaks at integer values of  $H$  and  $K$ , extensive diffuse scattering appears connecting Bragg reflections. The scattering is quasi-two dimensional and completely diffuse along  $L$ , generating structured planes of scattering perpendicular to  $(1, 1, 0)$  and equivalent reciprocal lattice directions.

Because the diffuse scattering in  $\text{PrCd}_3\text{P}_3$  shows the highest relative intensities, the stronger signal in  $\text{PrCd}_3\text{P}_3$  was chosen for analysis as representative of the behavior in all four compounds. Line-cuts of the diffuse scattering are presented along directions perpendicular [Fig. 4(b)] and parallel [Fig. 4(c)] to the planes of diffuse scattering for  $\text{PrCd}_3\text{P}_3$ . Additional line cuts for the other  $\text{LnCd}_3\text{P}_3$  are presented in Fig. S4 [66]. The line-cuts within the plane show that the diffuse plane is structured and peaked at half-integer positions, indicating a local breaking of translational symmetry.

The peak shapes were fit using a pseudo-Voigt profile, and the in-plane correlation lengths, extracted via the inverse of the full width at half maximum (FWHM) of the Lorentzian component of the profile, are shown in Figure 4(d,e). Correlation lengths as well as the intensity of the local correlations do not change significantly with temperature and are seemingly decoupled from thermally-induced atomic displacements, suggesting that the diffuse intensity arises from frustrated charge correlations within the trigonal planar CdP layer.

To further resolve the origin of the short-range charge correlations, 3D- $\Delta$ PDF analysis of the X-ray scattering data [67, 68] was performed using a modified approach to the punch-and-fill method [69]. A representative

$(H, K)$ -plane of the isolated diffuse scattering with the average structure removed and the real part of the Fourier transform are shown for  $\text{PrCd}_3\text{P}_3$  at  $T = 300$  K in Figure 5(b,c).

The vector probabilities of atomic displacements in the experimentally-derived 3D- $\Delta$ PDF are highest in intensity at integer lattice units in real space, corresponding to distances between like atoms in different unit cells. A quadrupole-like displacement feature appears at the first-nearest neighbor  $\langle 1, 0, 0 \rangle$  positions and another in-phase displacement correlation appears at the  $\langle 2, 0, 0 \rangle$  positions, indicative of strongly one-dimensional correlations along this direction. These correlations decay exponentially and have correlation lengths on the order of 5 unit cells, as demonstrated in Fig. S5 [66].

While the three Cd-P bond lengths in the CdP<sub>3</sub> layers are equal in the hexagonal cell, powder PDF results indicate one bond is shorter than the other two in the  $Cmc m$  cell. For instance, in the  $T = 80$  K  $\text{PrCd}_3\text{P}_3$  data, the shorter bonds are 2.42(11) Å, whereas the longer bond is 2.53(2) Å, representing an approximate 2% decrease/increase in the bond length with respect to the hexagonal cell. This distortion effectively reduces the CdP<sub>3</sub> trigonal planar units to one-dimensional CdP chains and maps the local distortion to a two-dimensional tiling of the honeycomb Cd-P network with “dimers”, where each dimer corresponds to the single long bond within each unit. This type of bond order is expected to be frustrated across the honeycomb network and is a likely candidate for the local correlations isolated in the 3D- $\Delta$ PDF analysis.

To assess the microscopic nature of these correlations, we employed forward Monte Carlo modeling to generate a large-box model with short-range correlations between sites on the CdP honeycomb lattice, the expected diffuse



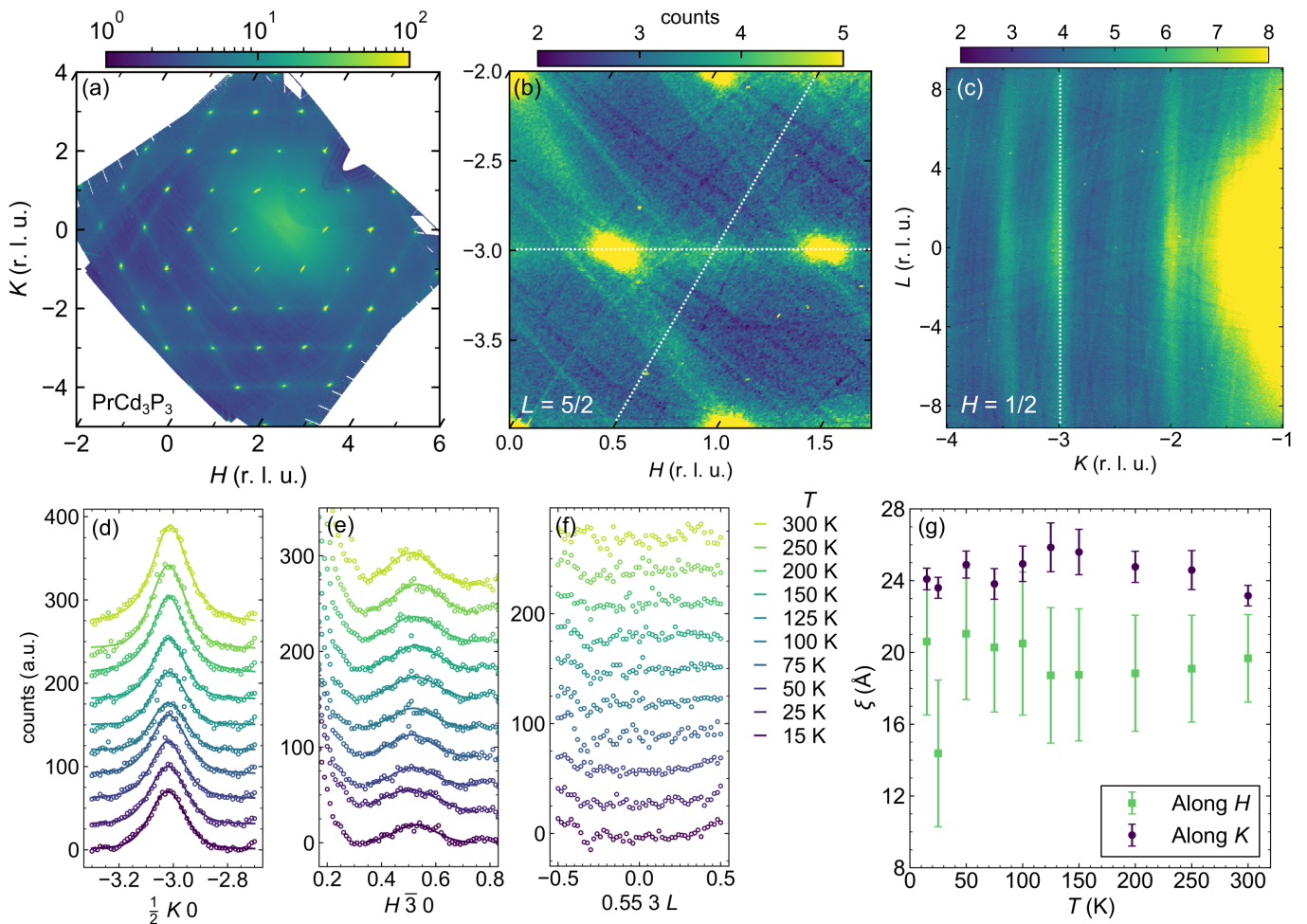


FIG. 4. (a) Single crystal X-ray diffraction data at  $T = 300$  K in the  $(H, K, 2)$  scattering plane for  $\text{PrCd}_3\text{P}_3$  revealing a complex diffuse scattering pattern between Bragg reflections that is representative of the  $L_n\text{Cd}_3\text{P}_3$  ( $L_n = \text{La}, \text{Ce}, \text{Nd}, \text{Pr}$ ) family.  $L = 2$  was selected for low background intensity. The large diffuse spot near the origin of the dataset is due to small-angle background scattering. (b) Line cut directions highlighted in a representative  $(H, K)$  scattering plane and (c)  $(K, L)$  scattering plane at  $T = 300$  K. (d) Peak shapes along the  $(\frac{1}{2}, K, 0)$  line cut and (e)  $(H, \bar{3}, 0)$  line cut, each fit using a Pseudovoigt profile and a linear background which was subtracted before plotting. (f) Line cut along  $L$  showing little to no modulation of the peak intensity along the interplane direction. A linear background was subtracted before plotting. (g) Correlation lengths obtained from the full width at half maximum of the fit profiles in the  $(H, K)$  plane reveal negligible temperature dependence along both directions.

scattering, and resulting  $\Delta\text{PDF}$  maps. The dimer covering of the honeycomb network is canonically defined such that each vertex of the honeycomb is reached by exactly one dimer. This problem can be mapped to a 2D Ising model on the (dual) triangular lattice [58, 59]. In this mapping, Ising spins decorate the center of each hexagon, and dimers are placed on those edges which sit between frustrated pairs of spins (up-up or down-down).

Within the dual model of Ising spins on an antiferromagnetic triangular lattice with couplings up to third nearest neighbor ( $J_1, J_2, J_3 < 0$ ), in the limit of large nearest neighbor  $J_1$ , frustration effects manifest one-dimensional “stripe” textures for  $J_3/J_2 < 0.5$  and “zig-zag” textures for  $J_3/J_2 > 0.5$  [70]. The stripe pattern in the Ising model maps to the “staggered” configuration in the dimer model, and the zig-zag pattern in the Ising

model maps to a “Herringbone”-like configuration of dimers on the honeycomb lattice (Fig. S6) [66, 71, 72]. The forward Monte Carlo model was built around the 2D Ising problem, and, after relaxing the spin configuration, the coordinates of each  $\text{Cd}_{\text{trig}}$  and  $\text{P}_{\text{trig}}$  site were modified to elongate one of the three Cd-P bonds for each  $\text{CdP}_3$  unit. The magnitude of these displacements were parameterized based on the orthorhombic  $Cmcm$  solution from the aforementioned small box modeling of the powder PDF data, though the model is not constrained by this symmetry.

By fixing a relatively large  $J_1$  and sweeping the ratio of  $J_3/J_2$  in the forward Monte Carlo simulation, we are able to tune the short-range correlations in a  $100 \times 100$  supercell between the staggered and Herringbone configurations of the dimer model (Fig. S7 [66]). Examination

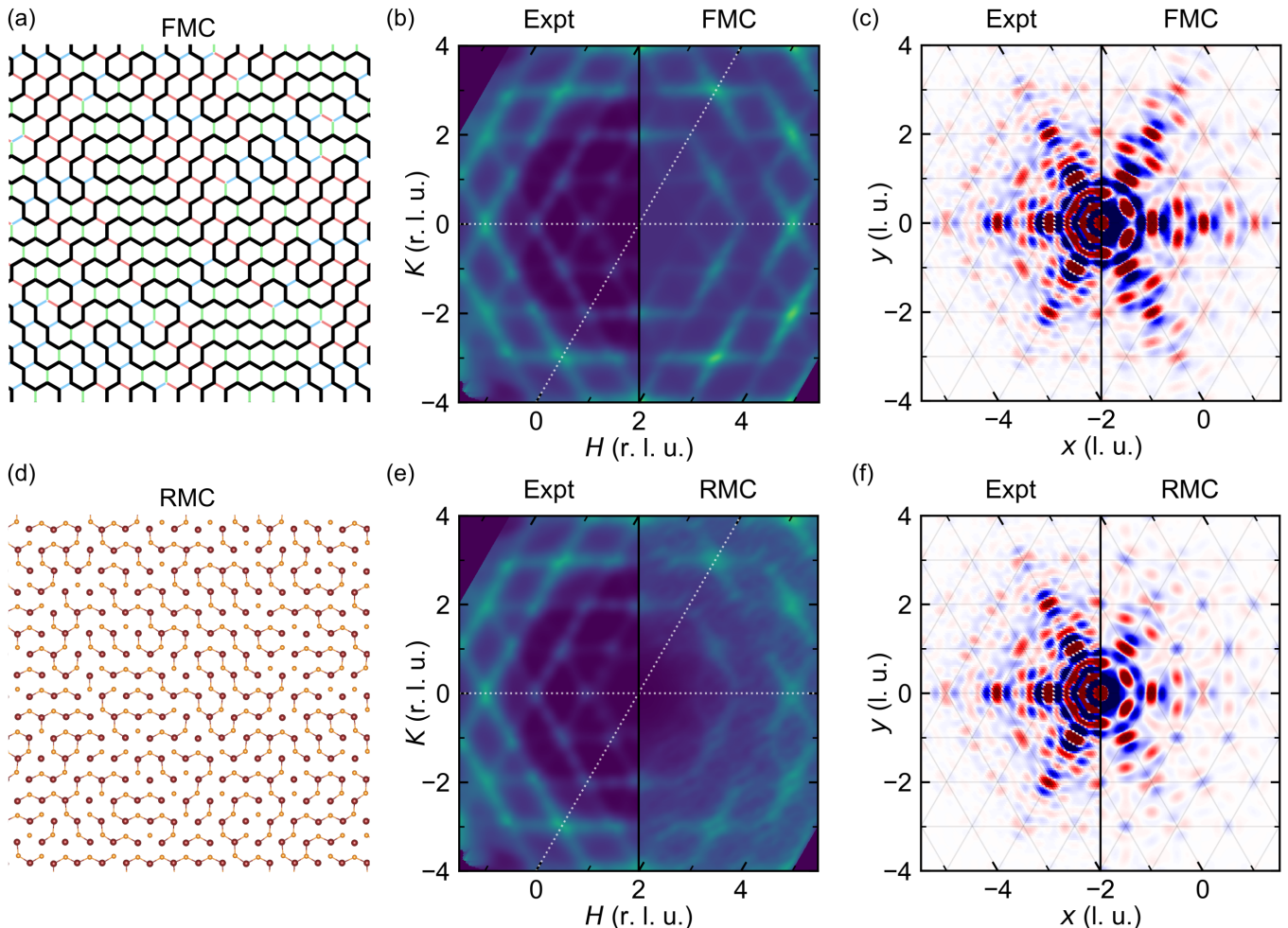


FIG. 5. (a) An example of the thermalized ground state resulting from the Forward Monte Carlo (FMC) simulation, revealing short-range, one-dimensional CdP chains. The three degenerate orientations of the long bond are highlighted in different colors, corresponding to the dimers in the forward Monte Carlo model. (b) Representative experimental data showing diffuse scattering in the  $(H, K, \frac{5}{2})$  scattering plane for  $\text{PrCd}_3\text{P}_3$  at  $T = 300$  K isolated by a modified punch-and-fill method, and the calculated diffuse scattering from the thermalized ground state of the FMC model. (c) The 3D- $\Delta$ PDF for  $\text{PrCd}_3\text{P}_3$  extracted from the diffuse scattering at  $T = 300$  K, and the 2D- $\Delta$ PDF resulting from the FMC model. (d) An example of the refined supercell configuration of CdP chains after reverse Monte Carlo (RMC) modeling using the  $(H, K, \frac{5}{2})$  scattering plane as the target. (e) Comparison of the experimental diffuse scattering and the calculated diffuse scattering from the refined RMC model. (f) Comparison of the experimental 3D- $\Delta$ PDF and the calculated 2D- $\Delta$ PDF obtained from the RMC model.

of the calculated diffuse scattering for each case reveals that the diffuse scattering planes observed in the experiment are closely replicated for  $J_3/J_2 \geq 0.5$ , and the experimentally observed half-integer maxima are recreated for  $J_3/J_2 > 0.5$  due to the nature of the symmetry lowering in the Herringbone configuration of dimers.

Optimized Monte Carlo scattering results are presented in Figure 5, where  $J_3/J_2 = 0.58$ . The resulting dimer model configuration shown in Figure 5(a) features an arrangement of one-dimensional CdP chains which are correlated over short length scales ( $\approx 3$  to 5 unit cells), with a weak tendency toward breaking translational symmetry by alternating chain direction. Due to the three-fold degeneracy of distortion pathways, three domains form, each rotated by  $120^\circ$  relative to the other

two. The calculated diffuse scattering that results from this short-range ordered supercell is shown in Figure 5(b). The planes of diffuse scattering, including the modulations in the structure factor and the weak half-integer maxima, are well-captured by the model. For further comparison, the 2D- $\Delta$ PDF transformation of this simulated scattering also agrees well with the corresponding 3D- $\Delta$ PDF transformation of the experimental scattering data [Fig. 5(c)], replicating the key features at integer coordinates in the experimental 3D- $\Delta$ PDF.

In order to further strengthen the interpretation presented in our model, reverse Monte Carlo modeling (RMC) was used to refine a large-box structural model against the experimental diffuse scattering. Because the scattering is completely diffuse along  $L$ , data from the

$(H, K, \frac{5}{2})$  scattering plane was used as the target for the RMC model. An  $75 \times 75 \times 1$  supercell including only a trigonal Cd-P plane was initialized with a random distribution of Cd and P distortions along directions A, B, and C [as defined in Fig. 1(d)], and each RMC move involved a swap of the displacement type of two randomly selected sites of the same element. The termination criteria was defined as 10 times the number of atoms in the supercell. The refined supercell, diffuse scattering, and  $\Delta$ PDF after convergence are shown in Figure 5(d-f). The RMC generally agrees with the results of the FMC model, replicating a similar chain correlation length and exhibiting a weak tendency to form chains which alternating directions. Taken together, the FMC and RMC results confirm that the origin of the diffuse scattering is bond-dependent, short-range interactions between Cd-P displacive distortions which follow the energy landscape enforced by frustrated bond order and result in a lower symmetry at the local scale.

## DISCUSSION AND CONCLUSIONS

In  $LnCd_3P_3$  compounds, the valence band maximum is composed primarily of phosphorus  $p$ -states, specifically from those P anions within the CdP layer [39]. The conduction band maximum is composed of cadmium  $s$ -states. Given that the  $Cd_{\text{trig}}$  cations are bonded solely to the three P anions within the CdP layer, the bonding interactions are therefore likely between  $Cd_{\text{trig}}$   $s$ -states and phosphorus  $p_x$  and  $p_y$  atomic orbitals. These atomic orbitals likely hybridize to enable a trigonal planar coordination environment.

In the ionic limit, any degree of charge transfer from the  $P^{3-}$  anions, which possess filled  $p_x$  and  $p_y$  bands (valence band maximum), to the trigonal planar  $Cd^{2+}$  cations, which possess empty  $Cd^{2+}$  states (conduction band minimum), will result in a second-order Jahn-Teller instability in the phosphorus  $p$ -states. Similarly, in the covalent limit, strong hybridization between the Cd  $s$ - and P  $p$ -states would result in  $sp^2$  hybridized orbitals, which would contain two holes and be subject to a first-order Jahn-Teller instability. In either scenario, a bonding instability is expected to arise from the unconventional trigonal planar  $CdP_3$  bonding environment.

The resulting bond instability generates local CdP chains within the honeycomb network whose configurations are governed via chemical bonding considerations – avoiding over- and under-bonded P ions. The effective interactions of this local bond order on a honeycomb lattice frustrate the formation of long-range order and map to the dual triangular lattice with Ising-like interactions [58, 59]. An alternative way to envision things is to consider local  $120^\circ$  displacements of Cd ions toward P ions in the honeycomb network. These displacement modes have a local Ising-like degree of freedom (toward or away) and can be mapped onto the midpoints of the CdP honeycomb bond network. This creates an emergent

kagome network that maps to the kagome-ice problem of antiferromagnetic Ising spins on a kagome lattice, and whose solution in the classical limit can be attained via dimer tiling on a honeycomb network [57].

Within the dual triangular lattice Ising model, extended interactions within a  $J_1 - J_2 - J_3$  model can generate a range of local patterns of order [70]. The “zig-zag” state accessed in the limit of appreciable antiferromagnetic  $J_3$  in the triangular lattice corresponds to the Herringbone local order of the dimer model revealed in reverse Monte Carlo analysis of the diffuse scattering in  $LnCd_3P_3$ . The resulting steric frustration is therefore similar to the frustrated charge order reported in  $ScV_6Sn_6$  [73, 74] and related kagome compounds [75–77] with an out-of-plane lattice chain instability. An unusual off-centering of the  $Cd_{\text{trig}}$  and  $As_{\text{trig}}$  ions was reported for similar  $LnCd_3As_3$  compounds, suggesting a generic in-plane instability for this entire class of materials and warrants further structural investigations [56].

The extended interactions mediated via a strain field imply a potentially rich set of states accessible via external strain in the  $LnCd_3P_3$  family of compounds. Pronounced strain effects and coupling of lattice fluctuations are known to couple to the charge order state and electronic properties of kagome materials with a similarly frustrated charge ordered state [78–81]. Given the narrow band gap of the  $LnCd_3P_3$  family, these compounds are likely dopable into a metallic state as well. Previous studies of  $LnCd_3P_3$  crystals grown via self-flux techniques indeed reported a weakly metallic state with a small carrier density [42]. Crystals grown via this method are likely self-doped (hole-doped) via excess phosphorus within the CdP blocks, but, curiously, the onset of metallic behavior coincides with the emergence of an unknown phase transition at high-temperature [42]. We propose this weak phase transition is a partial freezing of the frustrated bond-order native to the lattice, one whose frustration is relieved via the introduction of local charge carriers.

More generally, the ability to dope the  $LnCd_3P_3$  compounds opens a fascinating new frontier of exploring carrier tuning in a lattice hosting both strong magnetic and steric frustration. A quantum disordered magnetic ground state hosted within the local moments of the  $S_{eff} = 1/2 Ln$  layer can in principle be interfaced with the frustrated bond order within the  $CdP_3$  planes via charge carriers, potentially leading to a number of interesting effects. These could include giant magnetocaloric responses [82, 83] in the magnetic channel or emergent behavior, such as unconventional superconductivity [84, 85] within the charge channel. Future experiments on electronic symmetry breaking in carrier-doped  $LnCd_3P_3$  are therefore highly desired.

In conclusion, we have studied the  $LnCd_3P_3$  family of compounds and have identified a frustrated form of bond order akin to kagome-ice within its honeycomb, trigonal planar CdP layer. The bond frustration derives from a chain instability within the honeycomb network

and therefore maps to frustrated Ising spins on the dual triangular lattice. Signatures of this frustration persist to room temperature and exist independently from the magnetic frustration within the triangular lattice  $Ln$   $S_{\text{eff}} = 1/2$  moments. Our findings motivate future experiments probing the coupling between the two (bond and moment) frustrated networks as well as the impact of carrier doping as a means of stabilizing emergent phase behavior in this fascinating family of compounds.

#### ACKNOWLEDGEMENTS

SDW acknowledges helpful discussions with Leon Balents and Jacob Ruff. The authors acknowledge various forms of support from Casandra Gomez Alvarado, Guang Wu, Matt Krogstad, Dibyata Rout, and Joe Paddison. This work was supported by the US Department of Energy (DOE), Office of Basic Energy Sciences, Division of Materials Sciences and Engineering under Grant No. DE-SC0017752. S.J.G.A. acknowledges the additional financial support from the National Science Foundation Graduate Research Fellowship under Grant No. 1650114. J.R.C. acknowledges support through the NSF

MPS-Ascend Postdoctoral Fellowship (DMR-2137580). This research made use of the shared facilities of the NSF Materials Research Science and Engineering Center at UC Santa Barbara (DMR-2308708). Use was made of computational facilities purchased with funds from the National Science Foundation (CNS-1725797) and administered by the Center for Scientific Computing (CSC). The CSC is supported by the California NanoSystems Institute and the Materials Research Science and Engineering Center (MRSEC; NSF DMR-2308708) at UC Santa Barbara. G.P., B.R.O., and L.K. acknowledge support from the National Science Foundation (NSF) through Enabling Quantum Leap: Convergent Accelerated Discovery Foundries for Quantum Materials Science, Engineering and Information (Q-AMASE-i): Quantum Foundry at UC Santa Barbara (DMR-1906325). This research used resources of the Advanced Photon Source, a U.S. Department of Energy (DOE) Office of Science user facility operated for the DOE Office of Science by Argonne National Laboratory under Contract No. DE-AC02-06CH11357. Research conducted at the Center for High-Energy X-ray Sciences (CHEXS) is supported by the National Science Foundation (BIO, ENG and MPS Directorates) under award DMR-2342336.

- 
- [1] C. Broholm, R. J. Cava, S. A. Kivelson, D. G. Nocera, M. R. Norman, and T. Senthil, Quantum spin liquids, *Science* **367**, 10.1126/science.aay0668 (2020).
- [2] J. R. Chamorro, T. M. McQueen, and T. T. Tran, Chemistry of Quantum Spin Liquids, *Chem. Rev.* **121**, 2898–2934 (2020).
- [3] M. M. Bordelon, E. Kenney, C. Liu, T. Hogan, L. Posthuma, M. Kavand, Y. Lyu, M. Sherwin, N. P. Butch, C. Brown, M. J. Graf, L. Balents, and S. D. Wilson, Field-tunable quantum disordered ground state in the triangular-lattice antiferromagnet  $\text{NaYbO}_2$ , *Nat. Phys.* **15**, 1058–1064 (2019).
- [4] Y. Li, G. Chen, W. Tong, L. Pi, J. Liu, Z. Yang, X. Wang, and Q. Zhang, Rare-Earth Triangular Lattice Spin Liquid: A Single-Crystal Study of  $\text{YbMgGaO}_4$ , *Physical Review Letters* **115**, 167203 (2015).
- [5] Y. Li, H. Liao, Z. Zhang, S. Li, F. Jin, L. Ling, L. Zhang, Y. Zou, L. Pi, Z. Yang, J. Wang, Z. Wu, and Q. Zhang, Gapless quantum spin liquid ground state in the two-dimensional spin-1/2 triangular antiferromagnet  $\text{YbMgGaO}_4$ , *Scientific Reports* **5**, 16419 (2015).
- [6] J. A. M. Paddison, M. Daum, Z. Dun, G. Ehlers, Y. Liu, M. B. Stone, H. Zhou, and M. Mourigal, Continuous excitations of the triangular-lattice quantum spin liquid  $\text{YbMgGaO}_4$ , *Nature Physics* **13**, 117 (2017).
- [7] N. Li, A. Rutherford, Y. Y. Wang, H. Liang, Q. J. Li, Z. J. Zhang, H. Wang, W. Xie, H. D. Zhou, and X. F. Sun, Ising-type quantum spin liquid state in  $\text{PrMgAl}_{11}\text{O}_{19}$ , *Physical Review B* **110**, 134401 (2024).
- [8] Y. Cao, H. Bu, Z. Fu, J. Zhao, J. S. Gardner, Z. Ouyang, Z. Tian, Z. Li, and H. Guo, Synthesis, disorder and Ising anisotropy in a new spin liquid candidate  $\text{PrMgAl}_{11}\text{O}_{19}$ , *Materials Futures* **3**, 035201 (2024).
- [9] Z. Ma, S. Zheng, Y. Chen, R. Xu, Z.-Y. Dong, J. Wang, H. Du, J. P. Embs, S. Li, Y. Li, Y. Zhang, M. Liu, R. Zhong, J.-M. Liu, and J. Wen, Possible gapless quantum spin liquid behavior in the triangular-lattice Ising antiferromagnet  $\text{PrMgAl}_{11}\text{O}_{19}$ , *Physical Review B* **109**, 165143 (2024).
- [10] H. Bu, M. Ashtar, T. Shiroka, H. C. Walker, Z. Fu, J. Zhao, J. S. Gardner, G. Chen, Z. Tian, and H. Guo, Gapless triangular-lattice spin-liquid candidate  $\text{PrZnAl}_{11}\text{O}_{19}$ , *Physical Review B* **106**, 134428 (2022).
- [11] B. Gao, T. Chen, C. Liu, M. L. Klemm, S. Zhang, Z. Ma, X. Xu, C. Won, G. T. McCandless, N. Murai, S. Ohira-Kawamura, S. J. Moxim, J. T. Ryan, X. Huang, X. Wang, J. Y. Chan, S.-W. Cheong, O. Tchernyshyov, L. Balents, and P. Dai, Spin Excitation Continuum in the Exactly Solvable Triangular-Lattice Spin Liquid  $\text{CeMgAl}_{11}\text{O}_{19}$  (2024), 10.48550/arXiv.2408.15957.
- [12] B. R. Ortiz, P. M. Sarte, A. H. Avidor, A. Hay, E. Kenney, A. I. Kolesnikov, D. M. Pajerowski, A. A. Aczel, K. M. Taddei, C. M. Brown, C. Wang, M. J. Graf, R. Seshadri, L. Balents, and S. D. Wilson, Quantum disordered ground state in the triangular-lattice magnet  $\text{NaRuO}_2$ , *Nat. Phys.* **19**, 943–949 (2023).
- [13] B. Normand and A. M. Oleś, Frustration and entanglement in the  $t_{2g}$  spin-orbital model on a triangular lattice: Valence-bond and generalized liquid states, *Phys. Rev. B* **78**, 10.1103/physrevb.78.094427 (2008).
- [14] Y. Kitaoka, T. Kobayashi, A. Kōda, H. Wakabayashi, Y. Niino, H. Yamakage, S. Taguchi, K. Amaya, K. Yamaura, M. Takano, A. Hirano, and R. Kanno, Orbital Frustration and Resonating Valence Bond State in the Spin-1/2 Triangular Lattice  $\text{LiNiO}_2$ , *J. Phys. Soc. Jpn.* **67**, 3703–3706 (1998).



- [15] H. F. Pen, J. van den Brink, D. I. Khomskii, and G. A. Sawatzky, Orbital Ordering in a Two-Dimensional Triangular Lattice, *Phys. Rev. Lett.* **78**, 1323–1326 (1997).
- [16] P. W. Anderson, Ordering and antiferromagnetism in ferrites, *Phys. Rev.* **102**, 1008 (1956).
- [17] R. Seshadri, Lone pairs in insulating pyrochlores: Ice rules and high- $k$  behavior, *Solid State Sci.* **8**, 259 (2006).
- [18] B. C. Melot, R. Tackett, J. O'Brien, A. L. Hector, G. Lawes, R. Seshadri, and A. P. Ramirez, Large low-temperature specific heat in pyrochlore  $\text{Bi}_2\text{Ti}_2\text{O}_7$ , *Phys. Rev. B.* **79**, 224111 (2009).
- [19] P. W. Anderson, The Resonating Valence Bond State in  $\text{La}_2\text{CuO}_4$  and Superconductivity, *Science* **235**, 1196 (1987).
- [20] E. G. Moon and S. Sachdev, Underdoped cuprates as fractionalized Fermi liquids: Transition to superconductivity, *Physical Review B* **83**, 224508 (2011).
- [21] T. Senthil, S. Sachdev, and M. Vojta, Fractionalized Fermi Liquids, *Physical Review Letters* **90**, 216403 (2003).
- [22] T. Senthil, M. Vojta, and S. Sachdev, Weak magnetism and non-Fermi liquids near heavy-fermion critical points, *Physical Review B* **69**, 035111 (2004).
- [23] T. Senthil and P. A. Lee, Cuprates as doped  $U(1)$  spin liquids, *Physical Review B* **71**, 174515 (2005).
- [24] J. Custers, P. Gegenwart, G. Geibel, F. Steglich, P. Coleman, and S. Paschen, Evidence for a Non-Fermi-Liquid Phase in Ge-Substituted  $\text{YbRh}_2\text{Si}_2$ , *Physical Review Letters* **104**, 186402 (2010).
- [25] Y. Tokiwa, J. J. Ishikawa, S. Nakatsuji, and P. Gegenwart, Quantum criticality in a metallic spin liquid, *Nature Materials* **13**, 356 (2014).
- [26] Q. Si, Global magnetic phase diagram and local quantum criticality in heavy fermion metals, *Physica B: Condensed Matter Proceedings of the International Conference on Strongly Correlated Electron Systems*, **378-380**, 23 (2006).
- [27] S. Clarke, A. Fowkes, A. Harrison, R. Ibberson, and M. Rosseinsky, Synthesis, structure, and magnetic properties of  $\text{NaTiO}_2$ , *Chemistry of materials* **10**, 372 (1998).
- [28] T. McQueen, P. Stephens, Q. Huang, T. Klimczuk, F. Ronning, and R. J. Cava, Successive orbital ordering transitions in  $\text{NaVO}_2$ , *Physical review letters* **101**, 166402 (2008).
- [29] T. Chen, A. Ghasemi, J. Zhang, L. Shi, Z. Tagay, L. Chen, E.-S. Choi, M. Jaime, M. Lee, Y. Hao, H. Cao, B. Winn, R. Zhong, X. Xu, N. P. Armitage, R. Cava, and C. Broholm, Phase diagram and spectroscopic evidence of superconductivity in quantum ising magnet  $\text{K}_2\text{Co}(\text{SeO}_3)_2$  (2024), arXiv:2402.15869 [cond-mat.str-el].
- [30] L. Ding, P. Manuel, S. Bachus, F. Grußler, P. Gegenwart, J. Singleton, R. D. Johnson, H. C. Walker, D. T. Adroja, A. D. Hillier, and A. A. Tsirlin, Gapless spin-liquid state in the structurally disorder-free triangular antiferromagnet  $\text{NaYbO}_2$ , *Phys. Rev. B* **100**, 10.1103/physrevb.100.144432 (2019).
- [31] M. Baenitz, P. Schlender, J. Sichelschmidt, Y. A. Onykiienko, Z. Zangeneh, K. M. Ranjith, R. Sarkar, L. Hozoi, H. C. Walker, J.-C. Orain, H. Yasuoka, J. van den Brink, H. H. Klauss, D. S. Inosov, and T. Doert,  $\text{NaYbS}_2$ : A planar spin-1/2 triangular-lattice magnet and putative spin liquid, *Phys. Rev. B* **98**, 10.1103/physrevb.98.220409 (2018).
- [32] R. Sarkar, P. Schlender, V. Grinenko, E. Haeussler, P. J. Baker, T. Doert, and H.-H. Klauss, Quantum spin liquid ground state in the disorder free triangular lattice  $\text{NaYbS}_2$ , *Phys. Rev. B* **100**, 10.1103/physrevb.100.241116 (2019).
- [33] A. O. Scheie, E. A. Ghioldi, J. Xing, J. a. M. Paddison, N. E. Sherman, M. Dupont, L. D. Sanjeeva, S. Lee, A. J. Woods, D. Abernathy, D. M. Pajerowski, T. J. Williams, S.-S. Zhang, L. O. Manuel, A. E. Trumper, C. D. Pemmaraju, A. S. Sefat, D. S. Parker, T. P. Devereaux, R. Movshovich, J. E. Moore, C. D. Batista, and D. A. Tennant, Proximate spin liquid and fractionalization in the triangular antiferromagnet  $\text{KYbSe}_2$ , *Nature Physics* **20**, 74 (2024).
- [34] T. Xie, A. A. Eberharter, J. Xing, S. Nishimoto, M. Brando, P. Khanenko, J. Sichelschmidt, A. A. Turrini, D. G. Mazzone, P. G. Naumov, L. D. Sanjeeva, N. Harrison, A. S. Sefat, B. Normand, A. M. Läuchli, A. Podlesnyak, and S. E. Nikitin, Complete field-induced spectral response of the spin-1/2 triangular-lattice antiferromagnet  $\text{CsYbSe}_2$ , *npj Quantum Materials* **8**, 1 (2023).
- [35] P.-L. Dai, G. Zhang, Y. Xie, C. Duan, Y. Gao, Z. Zhu, E. Feng, Z. Tao, C.-L. Huang, H. Cao, A. Podlesnyak, G. E. Granroth, M. S. Everett, J. C. Neuefeind, D. Voneshen, S. Wang, G. Tan, E. Morosan, X. Wang, H.-Q. Lin, L. Shu, G. Chen, Y. Guo, X. Lu, and P. Dai, Spinon Fermi Surface Spin Liquid in a Triangular Lattice Antiferromagnet  $\text{NaYbSe}_2$ , *Physical Review X* **11**, 021044 (2021).
- [36] K. M. Ranjith, S. Luther, T. Reimann, B. Schmidt, P. Schlender, J. Sichelschmidt, H. Yasuoka, A. M. Strydom, Y. Skourski, J. Wosnitza, H. Kühne, T. Doert, and M. Baenitz, Anisotropic field-induced ordering in the triangular-lattice quantum spin liquid  $\text{NaYbSe}_2$ , *Physical Review B* **100**, 224417 (2019).
- [37] K. M. Ranjith, D. Dmytriieva, S. Kim, J. Sichelschmidt, S. Luther, D. Ehlers, H. Yasuoka, J. Wosnitza, A. A. Tsirlin, H. Kühne, and M. Baenitz, Field-induced instability of the quantum spin liquid ground state in the  $J_{\text{eff}} = \frac{1}{2}$  triangular-lattice compound  $\text{NaYbO}_2$ , *Physical Review B* **99**, 180401 (2019).
- [38] A. T. Nientiedt and W. Jeitschko, The Series of Rare Earth Zinc Phosphides  $R\text{Zn}_3\text{P}_3$  ( $R=\text{Y, La-Nd, Sm, Gd-Er}$ ) and the Corresponding Cadmium Compound  $\text{PrCd}_3\text{P}_3$ , *Journal of Solid State Chemistry* **146**, 478 (1999).
- [39] S. Higuchi, Y. Noshima, N. Shirakawa, M. Tsubota, and J. Kitagawa, Optical, transport and magnetic properties of new compound  $\text{CeCd}_3\text{P}_3$ , *Materials Research Express* **3**, 056101 (2016).
- [40] N. Kabeya, T. Sakamoto, K. Hara, Y. Hara, S. Nakamura, K. Katoh, and A. Ochiai, Competing Exchange Interactions in Lanthanide Triangular Lattice Compounds  $\text{LnZn}_3\text{P}_3$  ( $\text{Ln} = \text{La-Nd, Sm, Gd}$ ), *Journal of the Physical Society of Japan* **89**, 074707 (2020).
- [41] J. R. Chamorro, A. R. Jackson, A. K. Watkins, R. Seshadri, and S. D. Wilson, Magnetic order in the  $S_{\text{eff}} = 1/2$  triangular-lattice compound  $\text{NdCd}_3\text{P}_3$ , *Physical Review Materials* **7**, 094402 (2023).
- [42] J. Lee, A. Rabus, N. R. Lee-Hone, D. M. Broun, and E. Mun, The two-dimensional metallic triangular lattice antiferromagnet  $\text{CeCd}_3\text{P}_3$ , *Physical Review B* **99**, 245159 (2019).
- [43] W.-J. Hu, S.-S. Gong, W. Zhu, and D. N. Sheng, Competing spin-liquid states in the spin- $\frac{1}{2}$  Heisenberg model on the triangular lattice, *Physical Review B* **92**, 140403 (2015).
- [44] S. Feng, J. Zhao, Y. Yang, X. Cheng, C. Yuan, and X. Cheng, Structural, electronic, and optical properties

- and bond stiffness of  $\text{ScAl}_3\text{C}_3$ -type  $\text{LaCd}_3\text{P}_3$  phases: *ab initio* calculations, *Journal of Physics and Chemistry of Solids* **134**, 115 (2019).
- [45] A. Yamada, N. Hara, K. Matsubayashi, K. Munakata, C. Ganguli, A. Ochiai, T. Matsumoto, and Y. Uwatoko, Effect of pressure on the electrical resistivity of  $\text{CeZn}_3\text{P}_3$ , *Journal of Physics: Conference Series* **215**, 012031 (2010).
- [46] J. Kitagawa, Possible Phase Transition and Band Gap Closing in Photoexcited Semiconductor  $\text{CeZn}_3\text{P}_3$ , *Journal of the Physical Society of Japan* **82**, 125001 (2013).
- [47] J. Kitagawa, D. Kitajima, K. Shimokawa, and H. Takaki, Photoinduced Kondo effect in  $\text{CeZn}_3\text{P}_3$ , *Physical Review B* **93**, 035122 (2016).
- [48] Y. Ren, S. Feng, C. Yuan, X. Cheng, and Z. Li, First-principle study on  $\text{ScAl}_3\text{C}_3$ -type  $\text{LaCd}_3\text{P}_3$  phases under high pressure, *Modern Physics Letters B* **34**, 2050347 (2020).
- [49] S. R. Dunsiger, J. Lee, J. E. Sonier, and E. D. Mun, Long-range magnetic order in the anisotropic triangular lattice system  $\text{CeCd}_3\text{As}_3$ , *Physical Review B* **102**, 064405 (2020).
- [50] A. Ochiai, N. Kabeya, K. Maniwa, M. Saito, S. Nakamura, and K. Katoh, Field-induced anomalous magnetic state beyond the magnetically ordered state in the slightly distorted triangular  $S = \frac{1}{2}$  rare-earth antiferromagnet  $\text{CeZn}_3\text{P}_3$ , *Physical Review B* **104**, 144420 (2021).
- [51] O. P. Uzoh, S. Kim, and E. Mun, Influence of crystalline electric field on the magnetic properties of  $\text{CeCd}_3\text{X}_3$  ( $X = \text{P}, \text{As}$ ), *Physical Review Materials* **7**, 013402 (2023).
- [52] Y.-D. Li, X. Wang, and G. Chen, Anisotropic spin model of strong spin-orbit-coupled triangular antiferromagnets, *Physical Review B* **94**, 035107 (2016).
- [53] J. Saravanan, H. Ponmani, Y. Sato, J.-i. Hayashi, Y. Kawamura, H. Gotou, and C. Sekine, Magnetic Properties of Layered Rare-Earth Zinc Phosphide  $\text{HoZn}_3\text{P}_3$  Prepared under High Pressure, *Journal of the Physical Society of Japan* **90**, 094701 (2021).
- [54] A. Ochiai, K. Hara, F. Kikuchi, T. Inukai, E. Matsuoka, H. Onodera, S. Nakamura, T. Nojima, and K. Katoh, Quantum spin system in f-electron compounds - $\text{YbAl}_3\text{C}_3$  and its related compounds-, *Journal of Physics: Conference Series* **200**, 022040 (2010).
- [55] K. E. Avers, P. A. Maksimov, P. F. S. Rosa, S. M. Thomas, J. D. Thompson, W. P. Halperin, R. Movshovich, and A. L. Chernyshev, Fingerprinting triangular-lattice antiferromagnet by excitation gaps, *Physical Review B* **103**, L180406 (2021).
- [56] S. S. Stoyko and A. Mar, Ternary Rare-Earth Arsenides  $\text{REZn}_3\text{As}_3$  ( $\text{RE} = \text{La}-\text{Nd}, \text{Sm}$ ) and  $\text{RECd}_3\text{As}_3$  ( $\text{RE} = \text{La}-\text{Pr}$ ), *Inorganic Chemistry* **50**, 11152 (2011).
- [57] R. Moessner and S. L. Sondhi, Ising models of quantum frustration, *Phys. Rev. B* **63**, 224401 (2001).
- [58] T. M. Schlittler, R. Mosseri, and T. Barthel, Phase diagram of the hexagonal lattice quantum dimer model: Order parameters, ground-state energy, and gaps, *Physical Review B* **96**, 195142 (2017).
- [59] R. Moessner, S. L. Sondhi, and P. Chandra, Phase diagram of the hexagonal lattice quantum dimer model, *Physical Review B* **64**, 144416 (2001).
- [60] <https://topas.webspace.durham.ac.uk/>.
- [61] H. T. Stokes, D. M. Hatch, and B. J. Campbell, ISODIS-TORT, ISOTROPY software suite, <https://iso.byu.edu> (2023).
- [62] <https://github.com/nexpy/nxrefine>.
- [63] [https://github.com/stevenjgomez/nxs\\_analysis\\_tools](https://github.com/stevenjgomez/nxs_analysis_tools).
- [64] G. Savelsberg, Ternäre Pnictide und Chalkogenide von Alkalimetallen und IB- bzw. IIB-Elementen / On Ternary Pnictides and Chalkogenides of Alkaline Metals and IB-resp. II B-Elements, *Zeitschrift für Naturforschung B* **33**, 370 (1978), publisher: De Gruyter.
- [65] R. Vogel and H.-U. Schuster,  $\text{KHgAs}$  (Sb) und  $\text{KZnAs}$  - Ternäre Verbindungen mit modifizierter  $\text{Ni}_2\text{In}$ -Struktur/ $\text{KHgAs}$  (Sb) and  $\text{KZnAs}$  - Ternary Compounds in a Modified  $\text{Ni}_2\text{In}$ -Structure, *Zeitschrift für Naturforschung B* **35**, 114 (1980).
- [66] See Supplementary Material at [URL].
- [67] T. Weber and A. Simonov, The three-dimensional pair distribution function analysis of disordered single crystals: basic concepts, *Z. Kristallogr. Cryst. Mater.* **227**, 238–247 (2012).
- [68] M. Kobas, T. Weber, and W. Steurer, Structural disorder in the decagonal Al-Co-Ni. I. Patterson analysis of diffuse x-ray scattering data., *Phys. Rev. B* **71**, 10.1103/physrevb.71.224205 (2005).
- [69] S. Griffitt, M. Spaić, J. Joe, Z. W. Anderson, D. Zhai, M. J. Krogstad, R. Osborn, D. Pelc, and M. Greven, Local inversion-symmetry breaking in a bismuthate high- $T_c$  superconductor, *Nat. Comm.* **14**, 10.1038/s41467-023-36348-9 (2023).
- [70] A. Smerald, S. Korshunov, and F. Mila, Topological Aspects of Symmetry Breaking in Triangular-Lattice Ising Antiferromagnets, *Physical Review Letters* **116**, 197201 (2016).
- [71] Y. Miura, Y. Yasui, M. Sato, N. Igawa, and K. Kakurai, New-type phase transition of  $\text{Li}_2\text{RuO}_3$  with honeycomb structure, *Journal of the Physical Society of Japan* **76**, 033705 (2007).
- [72] G. Jackeli and D. I. Khomskii, Classical dimers and dimerized superstructure in an orbitally degenerate honeycomb antiferromagnet, *Phys. Rev. Lett.* **100**, 147203 (2008).
- [73] G. Pokharel, B. R. Ortiz, L. Kautzsch, S. J. Gomez Alvarado, K. Mallayya, G. Wu, E.-A. Kim, J. P. C. Ruff, S. Sarker, and S. D. Wilson, Frustrated charge order and cooperative distortions in  $\text{ScV}_6\text{Sn}_6$ , *Phys. Rev. Materials* **7**, 104201 (2023).
- [74] S. J. G. Alvarado, G. Pokharel, B. R. Ortiz, J. A. M. Paddison, S. Sarker, J. P. C. Ruff, and S. D. Wilson, Frustrated Ising charge correlations in the kagome metal  $\text{ScV}_6\text{Sn}_6$ , *Physical Review B* **110**, L140304 (2024).
- [75] H. Miao, T. T. Zhang, H. X. Li, G. Fabbri, A. H. Said, R. Tartaglia, T. Yilmaz, E. Vescovo, J.-X. Yin, S. Murakami, X. L. Feng, K. Jiang, X. L. Wu, A. F. Wang, S. Okamoto, Y. L. Wang, and H. N. Lee, Signature of spin-phonon coupling driven charge density wave in a kagome magnet, *Nature Communications* **14**, 6183 (2023).
- [76] A. Korshunov, A. Kar, C. Y. Lim, D. Subires, J. Deng, Y. Jiang, H. Hu, D. Călugăru, C. Yi, S. Roychowdhury, C. Shekhar, G. Barbarino, P. Törmä, C. Felser, B. A. Bernevig, and S. Blanco-Canosa, Pressure induced quasi-long-range  $\sqrt{3} \times \sqrt{3}$  charge density wave and competing orders in the kagome metal  $\text{FeGe}$  (2024), arXiv:2409.04325 [cond-mat.str-el].
- [77] D. Subires, A. Kar, A. Korshunov, C. A. Fuller, Y. Jiang, H. Hu, D. Călugăru, C. McMonagle, C. Yi, S. Roychowdhury, C. Shekhar, J. Stremper, A. Jana, I. Vobornik, J. Dai, M. Tallarida, D. Chernyshov, A. Bosak, C. Felser, B. A.

- Bernevig, and S. Blanco-Canosa, Frustrated charge density wave and quasi-long-range bond-orientational order in the magnetic kagome FeGe (2024), arXiv:2408.04452 [cond-mat.str-el].
- [78] M. Tuniz, A. Consiglio, G. Pokharel, F. Parmigiani, T. Neupert, R. Thomale, G. Sangiovanni, S. D. Wilson, I. Vobornik, F. Salvador, F. Cilento, D. D. Sante, and F. Mazzola, Strain-induced enhancement of the charge-density-wave in the kagome metal  $\text{ScV}_6\text{Sn}_6$  (2024), arXiv:2403.18046 [cond-mat.str-el].
- [79] J. M. DeStefano, E. Rosenberg, O. Peek, Y. Lee, Z. Liu, Q. Jiang, L. Ke, and J.-H. Chu, Pseudogap behavior in charge density wave kagome material  $\text{ScV}_6\text{Sn}_6$  revealed by magnetotransport measurements, npj Quantum Materials **8**, 65 (2023).
- [80] S. Cheng, Z. Ren, H. Li, J. S. Oh, H. Tan, G. Pokharel, J. M. DeStefano, E. Rosenberg, Y. Guo, Y. Zhang, *et al.*, Nanoscale visualization and spectral fingerprints of the charge order in  $\text{ScV}_6\text{Sn}_6$  distinct from other kagome metals, npj Quantum Materials **9**, 14 (2024).
- [81] S. Wu, M. L. Klemm, J. Shah, E. T. Ritz, C. Duan, X. Teng, B. Gao, F. Ye, M. Matsuda, F. Li, X. Xu, M. Yi, T. Birol, P. Dai, and G. Blumberg, Symmetry breaking and ascending in the magnetic kagome metal FeGe, Phys. Rev. X **14**, 011043 (2024).
- [82] J. Xiang, C. Zhang, Y. Gao, W. Schmidt, K. Schmalzl, C.-W. Wang, B. Li, N. Xi, X.-Y. Liu, H. Jin, *et al.*, Giant magnetocaloric effect in spin supersolid candidate  $\text{Na}_2\text{BaCo}(\text{PO}_4)_2$ , Nature **625**, 270 (2024).
- [83] J. Liu, T. Gottschall, K. P. Skokov, J. D. Moore, and O. Gutfleisch, Giant magnetocaloric effect driven by structural transitions, Nature materials **11**, 620 (2012).
- [84] H.-C. Jiang and S. A. Kivelson, High temperature superconductivity in a lightly doped quantum spin liquid, Physical Review Letters **127**, 097002 (2021).
- [85] P. A. Lee, From high temperature superconductivity to quantum spin liquid: progress in strong correlation physics, Reports on Progress in Physics **71**, 012501 (2007).

# Supplemental Information

## AVERAGE STRUCTURAL REFINEMENTS

TABLE S1. Structural and refinement parameters for  $LnCd_3P_3$  obtained using synchrotron powder X-ray diffraction at  $T = 300$  K and 5 K ( $T = 5$  K data was not collected for  $CeCd_3P_3$ ).

$T$	$LaCd_3P_3$		$CeCd_3P_3$	$PrCd_3P_3$		$NdCd_3P_3$	
	300 K	5 K	300 K	300 K	5 K	300 K	5 K
Lattice							
$a$ (Å)	4.294532	4.289074	4.279790	4.268984	4.264544	4.260452	4.256547
$c$ (Å)	21.088651	21.010235	20.988965	20.947783	20.883543	20.917044	20.844464
$Ln$							
$U_{11}$	0.00757	0.00256	0.00742	0.00614	0.00336	0.0099	0.00461
$U_{12}$	0.003785	0.00128	0.00371	0.00307	0.00168	0.00495	0.002305
$U_{33}$	0.01028	0.01028	0.01393	0.01833	0.01906	0.01505	0.01415
$Cd_{tet}$							
$z$	0.12814(3)	0.128	0.12764	0.12735	0.12714	0.12708	0.12674
$U_{11}$	0.01604	0.00414	0.01549	0.01657	0.00686	0.01694	0.00872
$U_{12}$	0.00802	0.00207	0.007745	0.008285	0.00343	0.00847	0.00436
$U_{33}$	0.00788	0.00687	0.01222	0.01326	0.0125	0.01297	0.00808
$Cd_{trig}$							
$U_{11}$	0.02475	0.03596	0.02533	0.02826	0.02769	0.02773	0.02448
$U_{12}$	0.012375	0.01798	0.012665	0.01413	0.013845	0.013865	0.01224
$U_{33}$	0.04703	0.01885	0.04872	0.0501	0.01695	0.05463	0.01439
$P_{tet}$							
$z$	0.5797(1)	0.5793	0.57869	0.57777	0.57688	0.57739	0.57609
$U_{11}$	0.00983	0.00674	0.00868	0.00843	0.01062	0.01299	0.01302
$U_{12}$	0.004915	0.00337	0.00434	0.004215	0.00531	0.006495	0.00651
$U_{33}$	0.02167	0.01251	0.01616	0.01661	0.01721	0.01431	0.01069
$P_{trig}$							
$U_{11}$	0.02346	0.03474	0.03287	0.0392	0.03564	0.03112	0.02137
$U_{12}$	0.004915	0.00456	0.016435	0.0196	0.01782	0.01556	0.010685
$U_{33}$	0.01001	0.02035	0.00824	0.01844	0.01221	0.01479	0.01614



## LOCAL STRUCTURAL REFINEMENTS

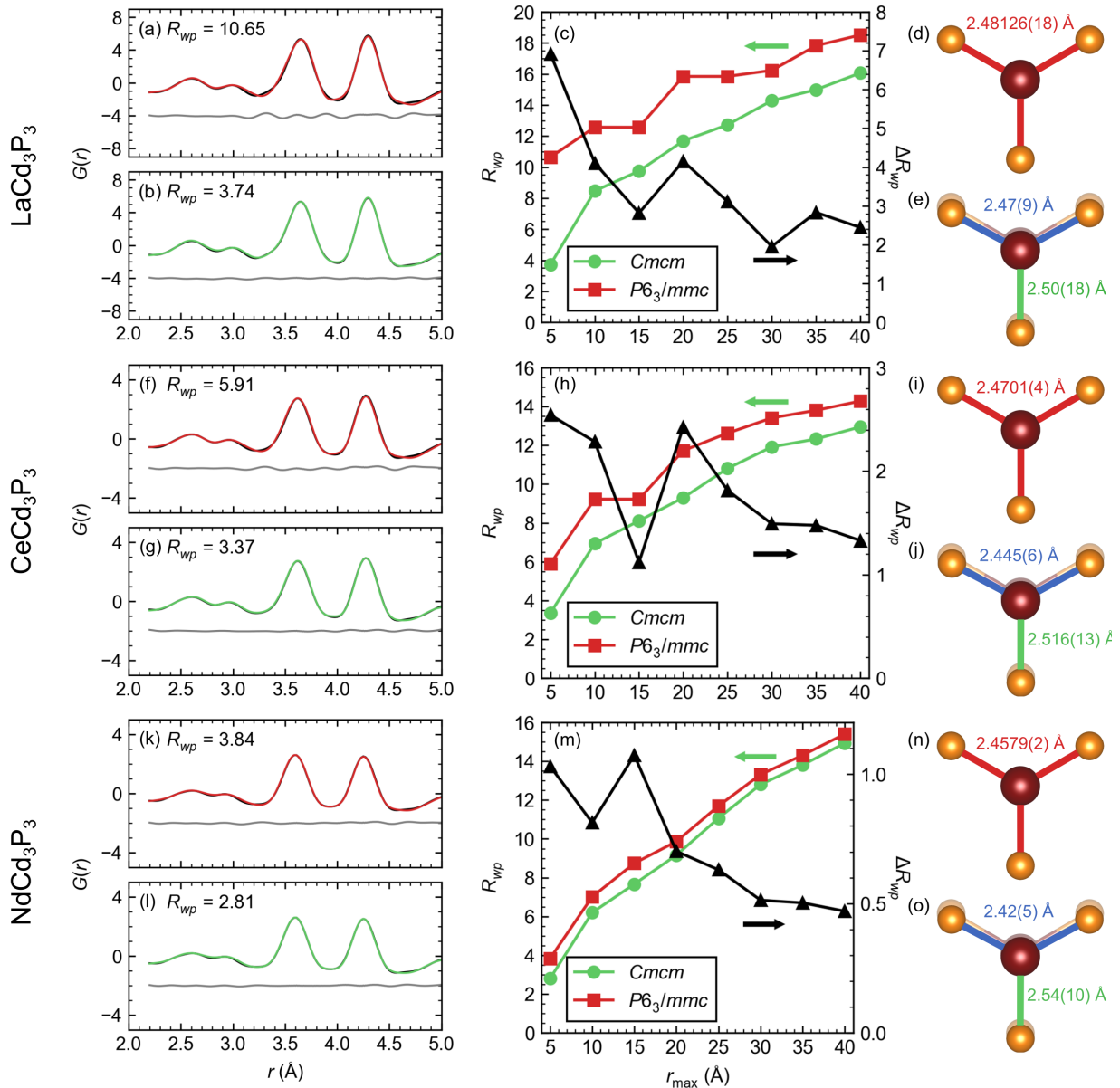


FIG. S1. Powder pair distribution function analysis for  $\text{LaCd}_3\text{P}_3$ ,  $\text{CeCd}_3\text{P}_3$ , and  $\text{NdCd}_3\text{P}_3$  at  $T = 80$  K. (a,f,k) Profile fit obtained from small-box modeling for the range  $2.2 \text{ \AA} < r < 5 \text{ \AA}$ , using the hexagonal  $P6_3/mmc$  cell and (b,g,l) the orthorhombic  $Cmcm$  cell. (c,h,m) Comparison of the  $R_{wp}$  values obtained over the ranges  $2.2 \text{ \AA} < r < r_{max}$  as a function of  $r_{max}$ . The right axis shows the difference between the  $Cmcm$  and  $P6_3/mmc$  fits for each  $r_{max}$ . (d,i,n) The refined bond lengths obtained from the  $P6_3/mmc$  and (e,j,o)  $Cmcm$  fits.

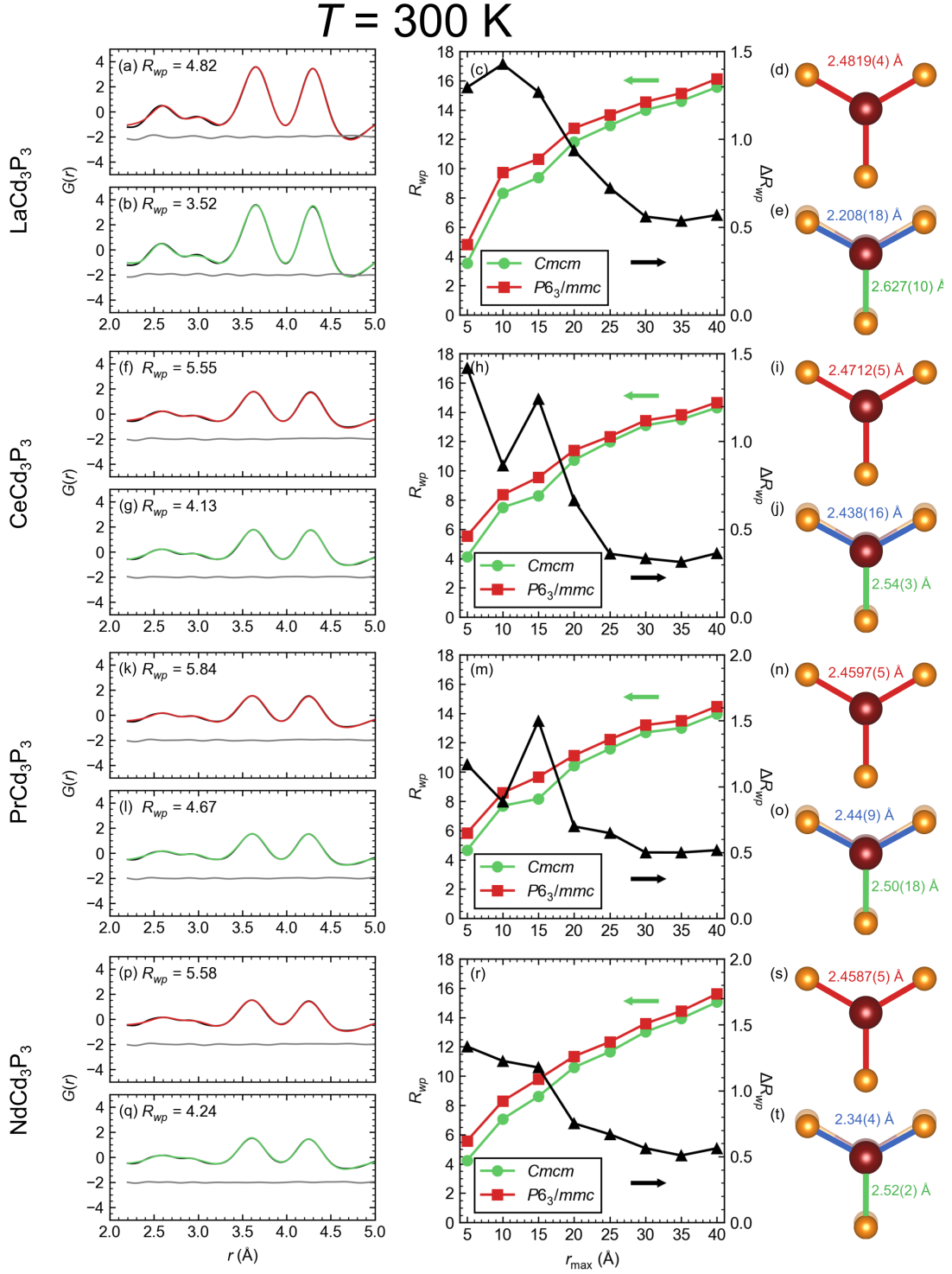


FIG. S2. Powder pair distribution function analysis for  $\text{LaCd}_3\text{P}_3$ ,  $\text{CeCd}_3\text{P}_3$ ,  $\text{PrCd}_3\text{P}_3$ , and  $\text{NdCd}_3\text{P}_3$  at  $T = 300 \text{ K}$ . (a,f,k,p) Profile fit obtained from small-box modeling for the range  $2.2 \text{ \AA} < r < 5 \text{ \AA}$ , using the hexagonal  $P6_3/mmc$  cell and (b,g,l,q) the orthorhombic  $Cmcm$  cell. (c,h,m,r) Comparison of the  $R_{wp}$  values obtained over the ranges  $2.2 \text{ \AA} < r < r_{\text{max}}$  as a function of  $r_{\text{max}}$ . The right axis shows the difference between the  $Cmcm$  and  $P6_3/mmc$  fits for each  $r_{\text{max}}$ . (d,i,n,s) The refined bond lengths obtained from the  $P6_3/mmc$  and (e,j,o,t)  $Cmcm$  fits.

## SINGLE CRYSTAL X-RAY DIFFRACTION DATASETS

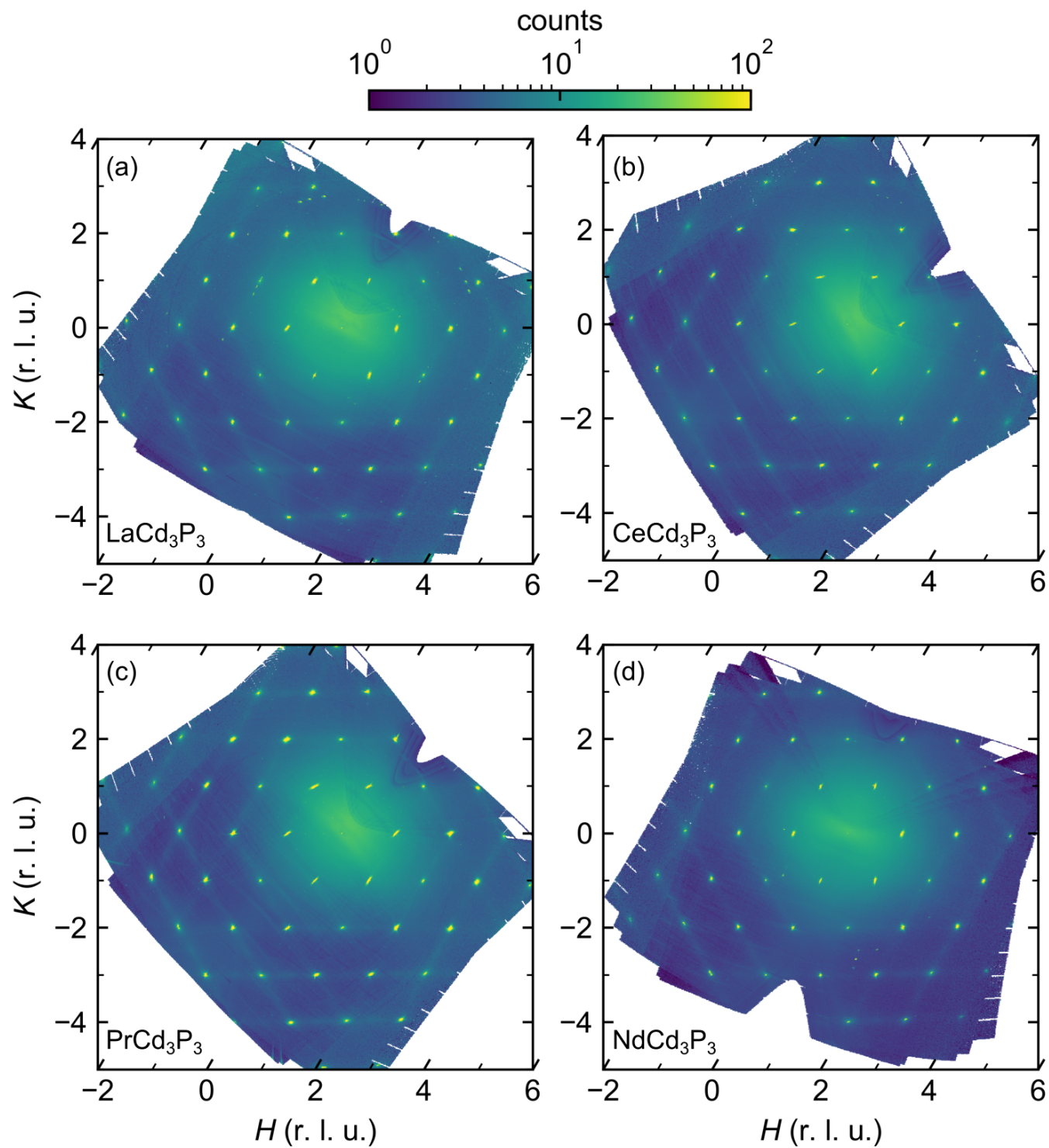
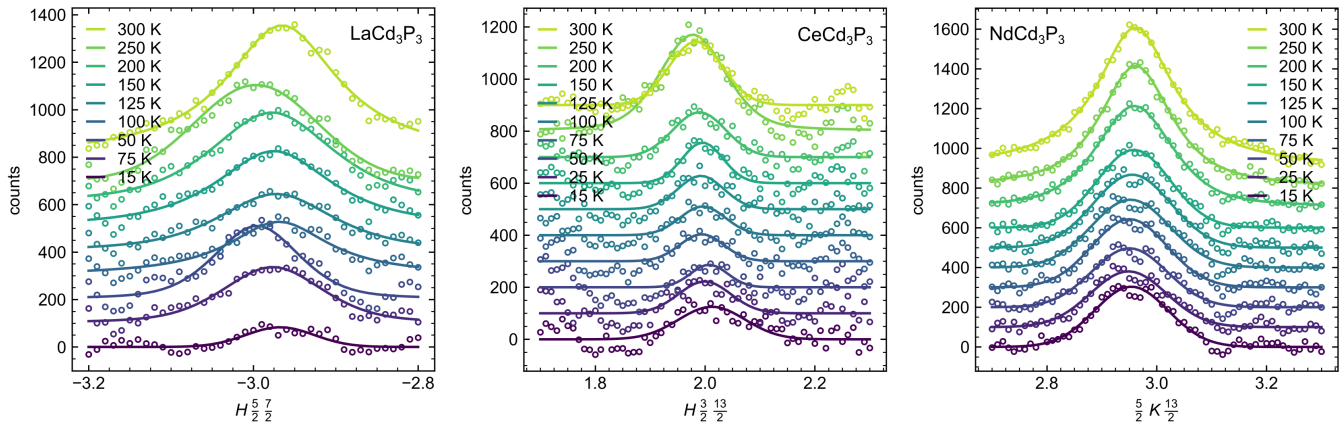
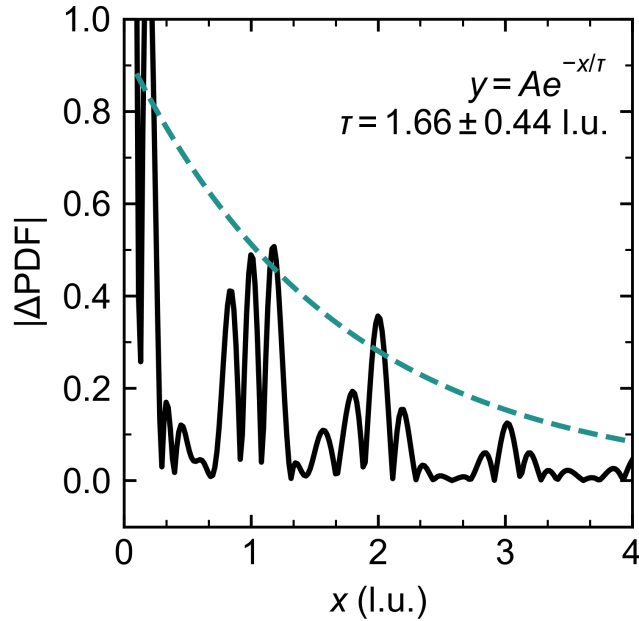


FIG. S3. Single crystal X-ray diffraction in the  $(H, K)$  scattering plane for (a)  $\text{LaCd}_3\text{P}_3$ , (b)  $\text{CeCd}_3\text{P}_3$ , (c)  $\text{PrCd}_3\text{P}_3$ , and (d)  $\text{NdCd}_3\text{P}_3$  at  $T = 300$  K.

## DIFFUSE SCATTERING ANALYSIS

FIG. S4. Linecuts perpendicular to the planes of diffuse scattering for other  $LnCd_3P_3$  compounds.3D- $\Delta$ PDF ANALYSISFIG. S5. Fit of  $|\Delta PDF|$  along the crystallographic  $a$  direction for  $PrCd_3P_3$  at  $T = 300$  K. An exponential decay model yields a decay constant of  $\tau = 1.66a \pm 0.44a$ , indicating that the signal decays significantly within 4-5 unit cells.



## FORWARD MONTE CARLO MODELING

## Dual triangular lattice antiferromagnetic Ising model

We employed the software DISCUS to perform forward Monte Carlo modeling based on the dual triangular lattice with Ising degrees of freedom on each site. A  $100 \times 100 \times 1$  supercell was initialized with an equal population of two distinct atom types representing the pseudospins. During each run, the structure was allowed to relax via random swapping of atom types between two sites along directions determined by correlation vectors specified by the user. The move is accepted if the energy is decreased, with a probability proportional to the pseudotemperature  $\text{temp}$ .

Occupational correlation vectors were specified for first- second- and third-nearest neighbors, using a fixed energy  $-J_1$ ,  $-J_2$ , and  $-J_3$ . A pseudotemperature  $\text{temp} = 1.0$  was used for all Monte Carlo simulations. The stopping criteria was defined as 500 times the number of sites in the supercell. After the Monte Carlo simulation thermalized, the Ising model was mapped back to the dimer model to generate a corresponding honeycomb layer of Cd-P with  $\text{Cd}_{\text{trig}}$  displaced towards a nearby P site if a dimer was present. For sites with overlapping dimers, one dimer was chosen at random and the other(s) discarded. The full experimental scattering volume was then simulated using the fourier section of DISCUS.

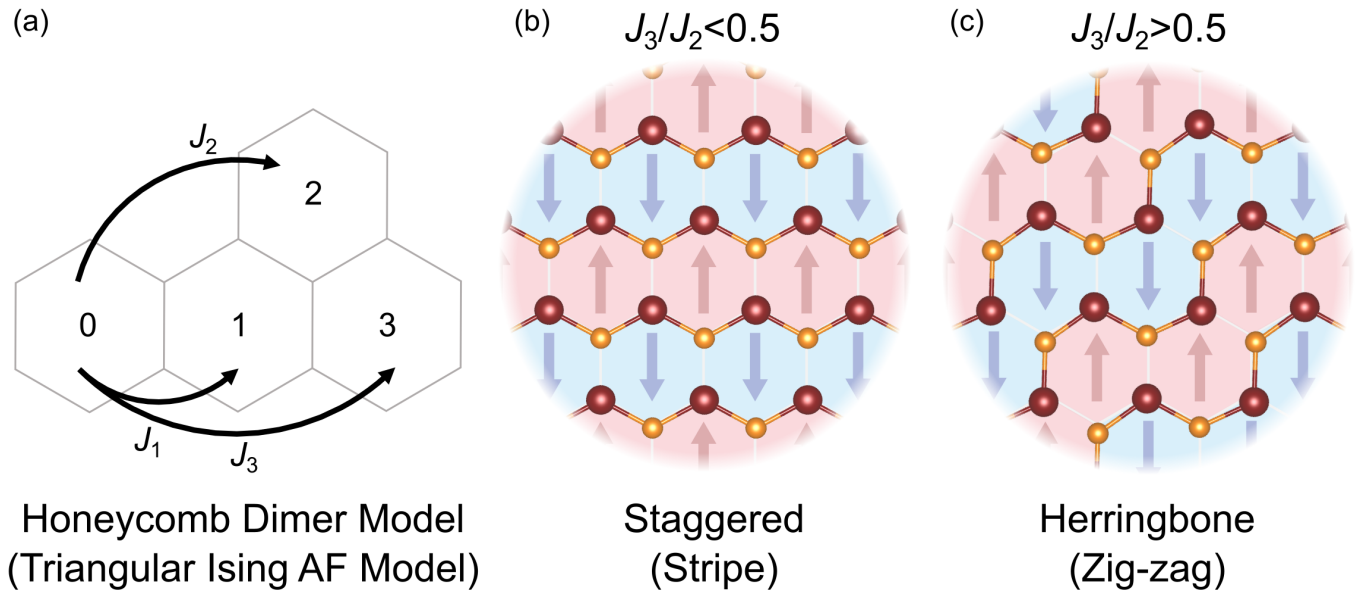


FIG. S6. The mapping between the honeycomb dimer model and the 2D triangular lattice antiferromagnetic Ising model. (a) The Hamiltonian underlying the Ising model involves three nearest neighbor interactions  $J_1$ ,  $J_2$ , and  $J_3$ . (b) In the limit  $J_1 \rightarrow -\infty$ , the dimers (spins) form a staggered (stripe) pattern for  $J_3/J_2 < 0.5$ , and (c) a Herringbone (zig-zag) pattern for  $J_3/J_2 > 0.5$ . In each case, the dimer maps to the single long bond within each  $\text{CdP}_3$  unit.

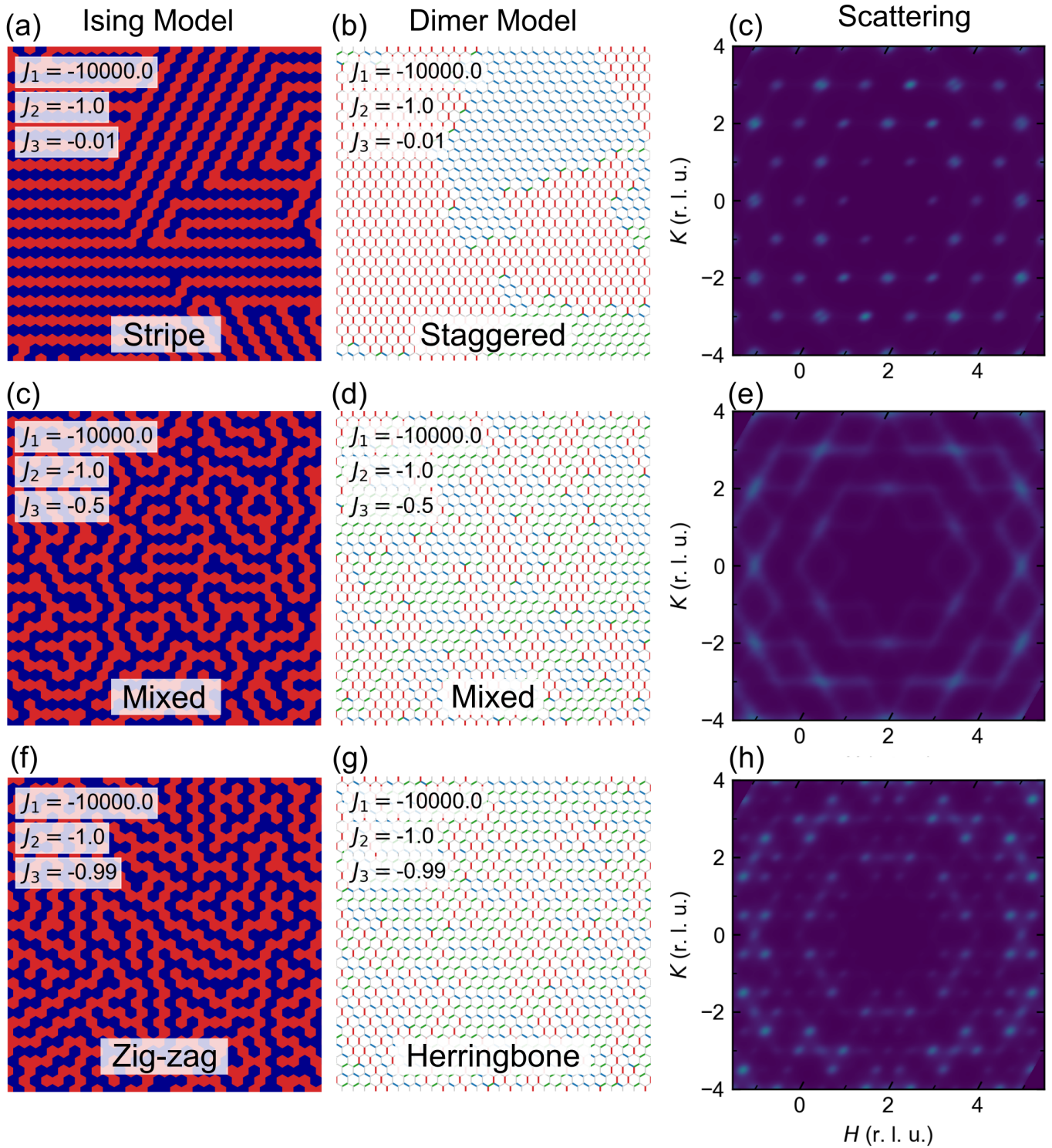


FIG. S7. Results from the forward Monte Carlo modeling. (a,e,f) The relaxed ground state of the Ising model obtained from the Monte Carlo simulation, with the interaction parameters printed in the inset. (b,d,g) The corresponding dimer state, and (c,e,h) the calculated diffuse scattering in the  $(H, K)$  plane.

### Three-State Potts model

Here we provide an alternative Hamiltonian which captures the observed short-range order via a three-state Potts model on a triangular lattice. Distortions were parameterized based on the orthorhombic  $Cmcm$  cell from the small box modeling of the powder PDF data, though the model is not constrained by this symmetry. The Monte Carlo model assigns each  $\text{Cd}_{\text{trig}}$  one of three possible distortions towards a nearest neighbor P site and was informed by chemical bonding considerations, including an energy penalty for creating under-bonded or over-bonded P sites. This places constraints on the relative distortion directions of the first coordination shell of local Cd atoms around each P. Due to the triangular geometry of the network, these constraints are direction-dependent. The following Hamiltonian, derived from the three-state Potts model, captures the resulting correlations along the three directions connecting Cd sites:

$$\hat{H}_1 = J_1 \sum_{n.n.} |\epsilon_{ijk}| \quad (1)$$

where the sum is performed over nearest neighbor ( $n.n.$ ) sites only. The index  $i$  corresponds to the crystallographic directions  $\langle 0, 1, 0 \rangle$ ,  $\langle 1, 1, 0 \rangle$ , and  $\langle 1, 0, 0 \rangle$ , respectively, for  $i = 1, 2, 3$ . The indices  $j$  and  $k$ , which also take the values  $j, k = \{1, 2, 3\}$ , encode the distortion directions A, B, and C on each of the two neighboring sites, as defined in Figure 1(d). When  $J_1 > 0$  this Hamiltonian enforces an energy penalty for neighboring pairs which leave a phosphorous atom either under- or over-bonded.

To capture the translational symmetry breaking that underlies the observed half-integer peak in the diffuse scattering along  $H$  and  $K$ , a second term promoting the formation of alternating stripes was necessary. This term  $\hat{H}_2$  also follows the same direction-dependent chemical bonding penalties, albeit perpendicular to the correlations promoted by  $\hat{H}_1$ .  $\hat{H}_2$  then takes the form

$$\hat{H}_2 = J_2 \sum_{n.n.} \delta_{ik}(1 - \delta_{ij}) \quad (2)$$

where  $|J_2| < |J_1|$ . The  $J_2 < 0$  regime favors the formation of a Herringbone pattern.

A  $180 \times 180 \times 1$  supercell was initialized with a random distribution and equal population of each of the three Cd displacements. The magnitude of these displacements was fixed during the Monte Carlo simulation, and corresponded to the displacement obtained from the refinement of our fit to the powder PDF data. Nearest neighbor Cd sites were allowed to switch displacement directions during the simulation. During each run, the interaction terms  $J_1$  and  $J_2$  were fixed and the system was allowed to thermalize into a low energy state.  $J_1$  and  $J_2$  were computationally refined over many runs to achieve a target correlation coefficient for each term in the Hamiltonian. The correlation coefficient is given by

$$c_{ij} = \frac{P_{ij} - \theta^2}{\theta(1 - \theta)} \quad (3)$$

where  $P_{ij}$  is the joint probability that neighboring Cd sites  $i$  and  $j$  possess the same distortion (of the two distortions corresponding to each crystallographic direction), and  $\theta$  is the overall fractional population of the distortion.

The simulations that most closely reproduced the experimental results had target correlation coefficients  $c_{12} = 0.5$  along  $[100]$ ,  $c_{23} = 0.5$  along  $[010]$ , and  $c_{31} = 0.5$  along  $[110]$ , corresponding to the interactions defined in  $\hat{H}_1$ , and coefficients  $c_{23} = -0.1$  along  $[100]$ ,  $c_{31} = -0.1$  along  $[010]$ , and  $c_{12} = -0.1$  along  $[110]$ , corresponding to the interactions defined in  $\hat{H}_2$ . The positive (negative)  $c_{ij}$  in each case corresponds to (anti)ferroelectric-like correlations between neighboring sites.

The resulting supercell generated from this forward Monte Carlo model features one-dimensional CdP chain correlations over short length scales (3-5 unit cells), nearly identical to the results obtained from the Ising/dimer model.